

Planetary Nebulae in the Circumnuclear Region of M31: A Spectroscopic Sample

Anqi Li^{1,2}, Zhiyuan Li^{1,2}, Hui Dong³, Xuan Fang^{4,5*}, Xiao-Jie Xu^{1,2}

¹ *School of Astronomy and Space Science, Nanjing University, Nanjing 210046, China;
lizy@nju.edu.cn*

² *Key Laboratory of Modern Astronomy and Astrophysics (Nanjing University), Ministry of Education, Nanjing 210046, China*

³ *Instituto de Astrofísica de Andalucía (CSIC), Glorieta de la Astronomía S/N, 18008, Granada, Spain*

⁴ *Laboratory for Space Research, Faculty of Science, University of Hong Kong, Pokfulam Road, Hong Kong, China*

⁵ *Department of Earth Sciences, Faculty of Science, University of Hong Kong, Pokfulam Road, Hong Kong, China*

ABSTRACT

Planetary nebulae (PNe) are an important tool for studying the dynamics and chemical evolution of galaxies in the Local Universe, given their characteristic, bright emission line spectra. The Andromeda Galaxy (M31) provides a unique laboratory for studying PNe in the circumnuclear region, thanks to its proximity and almost uniformly low line-of-sight extinction that ensures observations with high resolution and sensitivity. Using the WIYN/Hydra multi-fiber spectrograph, we have obtained optical (4119–6882 Å) spectra of 77 PN candidates selected from *Hubble Space Telescope* narrow-band imaging, which are located within the central ~ 500 pc region of M31. Among these candidates, 49 (64%) are spectroscopically observed for the first time. The spectra of 300 previously known PNe and H II regions, which primarily reside in the disk, are also taken for comparison. All 77 circumnuclear PN candidates exhibit prominent emission lines, including [O III] $\lambda 5007$, [N II] $\lambda 6583$, H α and H β , strongly suggesting that they are genuine PNe. We measured the line fluxes, radial velocities and line widths for all objects, and found that the radial velocities of the circumnuclear PNe generally trace rotation of the inner bulge. We also estimated a dynamical mass of $\sim 6.4 \pm 0.5 \times 10^9 M_{\odot}$ enclosed within an effective galactocentric radius of 340 pc, which is compatible with the previously estimated total stellar mass in this region.

* Visiting Astronomer, Key Laboratory of Optical Astronomy, National Astronomical Observatories, Chinese Academy of Sciences (NAOC), 20A Datun Road, Chaoyang District, Beijing 100101, China

Subject headings: planetary nebulae: general–galaxies: individual (M 31)

1. Introduction

Planetary nebulae (PNe) are the end products of the evolution of low- and intermediate-mass ($\sim 1\text{--}8 M_{\odot}$) stars. At this stage, the stars eject metal-rich materials into the interstellar medium (ISM), which is a fundamental process in the chemical evolution of galaxies (Kwok 2000). The stellar ejecta is ionized by ultraviolet (UV) photons from the central hot stars, producing significant emission lines, in particular [O III], [N II] and $H\alpha$ (Kwok 2000; Osterbrock & Ferland 2006), which provide useful diagnostics for the stellar metallicity (e.g., Delgado-Inglada 2016). When found in galactic spheroids, PNe can also serve as a robust tracer of stellar kinematics by using their radial velocities derived from the emission lines, and consequently a useful probe of the dynamical mass (e.g., Merrett et al. 2006; Coccato et al. 2009; Herrmann & Ciardullo 2009).

To date, PN candidates have been routinely identified in nearby, typically early-type, galaxies out to a distance of tens of Mpc, often through their bright [O III] $\lambda 5007$ nebular emission line (e.g., Ciardullo et al. 2004; Coccato et al. 2009; Sarzi et al. 2011; Longobardi et al. 2015a,b), which can reprocess up to $\sim 10\%$ of the central star’s bolometric luminosity (Dopita et al. 1992; Schönberner et al. 2010). However, identification of PNe in galactic nuclei, where strong stellar background is present, has proven a challenging task. PN surveys have been conducted to within the innermost ~ 100 pc of M81 (Jacoby et al. 1989), NGC 5128 (Walsh et al. 1999; Peng et al. 2004; Walsh et al. 2015), M33 (Ciardullo et al. 2004) and NGC 5102 (McMillan et al. 1994), offering insight to the dynamics and metallicity in the unique environment of galactic nuclei.

Thanks to its proximity (785 kpc, where $1''$ corresponds to 3.8 pc; McConnachie et al. 2005), which effectively reduces the stellar background within an imaging pixel, and its uniformly low line-of-sight extinction ($A_V \lesssim 0.5$; Dong et al. 2016), M 31 holds promise for identifying circumnuclear PNe with high-resolution, high-sensitivity optical imaging and spectroscopy. Several spectroscopic surveys for PNe in M31 have been conducted. The narrow-band survey of Ciardullo et al. (1989) found 429 PNe in the bulge, but follow-up spectroscopic observations (Richer et al. 1999; Jacoby & Ciardullo 1999) were only focused on the brightest ones. Halliday et al. (2006) presented velocities for a sample of 723 PNe in the disk and bulge, based on the [O III] $\lambda 4959, 5007$ doublet obtained by the WYFFOS fibre spectrograph with a spectral resolution of 0.9 \AA . Merrett et al. (2006; hereafter MMD06) conducted a survey of [O III] $\lambda 5007$ emission line objects, using the Planetary Nebula Spectrograph (PN.S) with a spectral resolution of 1.85 \AA , and catalogued 2615 PN candidates. Sanders et al. (2012) presented a spectroscopic follow-up of the PNe in MMD06 and

Halliday et al. (2006), and derived the metallicity profile along the disk. Their observations were taken by the MMT/Hectospec multi-fiber spectrograph, with a wide wavelength range of 3650–9200 Å and a modest spectral resolution of 5 Å. Using LAMOST spectroscopic data, Yuan et al. (2010) discovered tens of PNe in the outskirts of M31. However, the majority of the above objects reside in the disk and outer bulge/halo of M31; only a few tens of PNe were found within the central 500 pc. On the other hand, using the SAURON integral-field spectroscopic observation, Pastorello et al. (2013) identified 12 PN candidates within a projected distance of 21'' (~ 80 pc) from the center of M31, again through the detection of [O III] λ 5007. This work, however, suffered from a small field-of-view and low spatial resolution, thus only revealing the brightest PNe in this very central region.

Recently, we carried out an *HST*/WFC3 program to map diffuse, ionized gas in the circumnuclear region of M31 (Dong et al. 2014, 2016). Combining the WFC3/F502N and WFC3/F547M images obtained in this program, we have identified a total of 249 PN candidates located within a projected galactocentric radius of ~ 500 pc, the majority of which are new identifications (A. Li et al. 2018, in preparation; hereafter Paper I). In this work, we present the results of follow-up optical spectroscopy for 77 PN candidates, using the WIYN/Hydra multi-object spectrograph. In Section 2, we describe our sample selection, observations and data reduction. In Section 3, we analyze the most prominent emission lines detected in the spectra; these candidates are identified to be genuine PNe based on these emission lines, and their individual and statistical properties are derived, including line ratios and kinematics. In Section 4, we discuss the implications of this sizable sample of circumnuclear PNe. We draw our conclusions in Section 5. Throughout this work, we quote errors at the 1σ (68.3%) confidence level, unless otherwise stated.

2. Observations and Data Preparation

2.1. Sample selection

In Paper I, we have identified 249 PNe candidates in the circumnuclear region of M31, by contrasting the *HST* WFC3/UVIS F502N and F547M images. These candidates, hereafter referred to as HPNe, serve as the foremost sample for the follow-up spectroscopy. To facilitate a comparison with the PN population in the outer regions, we also added to our target list the 500 brightest objects (sorted by the apparent magnitude $m_{\lambda 5007}$) in the MMD06 catalog (hereafter MMDOs), which primarily consist of PNe, but also contain a small number of H II regions. The galactocentric radii of our targets thus range from 10 pc to 10 kpc (Figure 1).

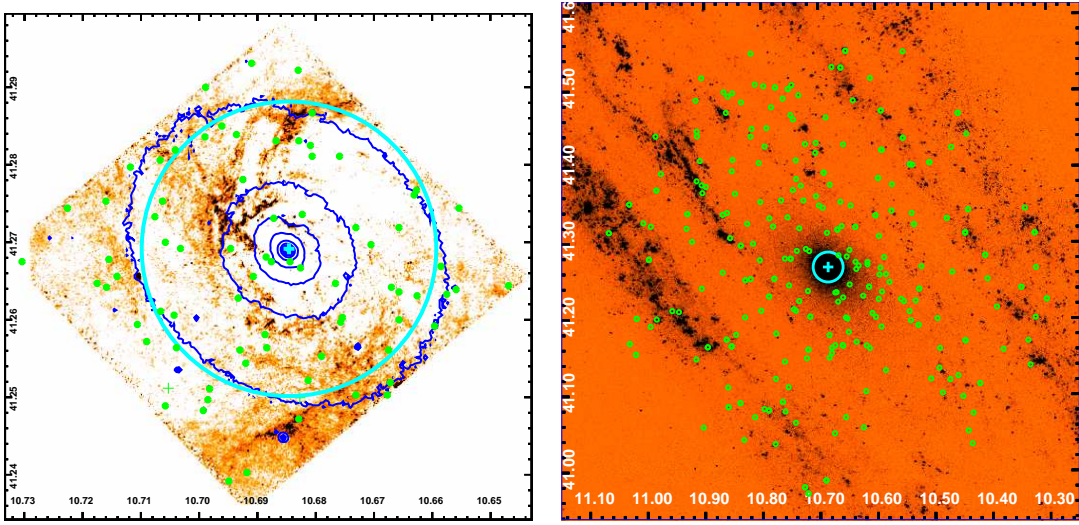


Fig. 1.— Left panel: An intensity map of diffuse H α emission obtained from *HST* WFC3/F656N image (Z. Li et al. in preparation). 77 PN candidates in this paper are marked with green circles. The blue contours outline the intensity distribution of the stellar bulge of M31. Right panel: GALEX far-UV image of M31 (Gil de Paz et al. 2007). The 300 MMDOs observed by WIYN/Hydra are marked with green circles. In both panels, darker color means higher surface brightness. The center of M31 is marked by a cyan cross, and cyan circles in both panels have a radius of $70''$ (~ 267 pc). HPNe detected within this radius are used for dynamical mass estimate of the bulge (Section 4.3). The X- and Y-axes are RA and DEC, in epoch 2000, respectively.

2.2. WIYN/Hydra observations

On 2014 October 3 and 2016 September 30, we observed the targets using the multi-object spectrograph, Hydra, on the 3.5m WIYN telescope (Barden & Armandroff 1995) at Kitt Peak. The focal plane of Hydra corresponds to a circle of 1° -diameter on the sky, which, at the time of the observations, could accommodate up to 90 fibers in a single field. The observations used the red fibers of $2''$ -diameter, which feed the Bench spectrograph with the 600 lines mm^{-1} grating. The wavelength coverage was $4119 \text{ \AA} - 6882 \text{ \AA}$, with a FWHM resolution of 3.35 \AA .

All observed fields were centered at the position of the M 31 nucleus. We used fiber-assignment program *hydra* from WIYN observatory to assign fiber positions. Due to the minimally allowed angular separation ($37''$) between any two fibers, crowding of the HPNe limits the observing efficiency in a single field. In each field, most fibers were positioned to cover a PN, and a few fibers were devoted to “random sky” positions to determine the sky background. While this choice limits our ability to accurately determining the immediate background of the HPNe (see further discussion in Section 3.1), this ensures a good observing efficiency. Hence we took a total of 8 fields to cover 77 HPNe ($\sim 30\%$ of our entire candidate list), with priority given to the brighter (in terms of m_{5007}) ones. In addition, a total of 300 MMDOs were covered in these fields, among which 267 have been classified as PNe and 33 as HII regions by MMD06. Figure 1 illustrates the target positions. The exposure time varied between $3 \times 1200 \text{ s}$, $4 \times 1200 \text{ s}$ or $3 \times 1800 \text{ s}$, depending on the presumed [O III] $\lambda 5007$ magnitude of the targets (Paper I). Several spectroscopic standard stars were also observed between the science exposures, for flux calibration. A log of the Hydra observations is given in Table 1.

Data reduction followed the standard procedure involving several IRAF[†] tasks. First, we used the *ccdproc* command in the *ccdred* package for image trimming, de-bias and dark current corrections. The data were then combined using *imcombine* in the *immatch* package to remove cosmic-rays and hot pixels. The *dohydra* task was then applied for spectral extraction, pixel-response correction and wavelength calibration. The *sarith* application in the *onedspec* package was then used for fiber-responding calibration. The mean sky spectra obtained with the sky fibers were subtracted from the target spectra using *skysub* in the *imred* package. This procedure was generally sufficient for the MMDOs. The HPNe, however, were immersed in the inner bulge where a substantial surface brightness gradient exists. Therefore, we conducted a “second subtraction” procedure to deal with the inhomogeneous stellar background, which will be further addressed in Section 3.1.

We tested the accuracy of our wavelength calibration by comparing the centroids of $\text{H}\alpha$ and $\text{H}\beta$ lines in the spectra of the MMDOs, each fitted independently with a Gaussian profile (Section 3.1). As illustrated in Figure 2, the derived radial velocities of $\text{H}\alpha$ and $\text{H}\beta$ are in excellent agreement,

[†]IRAF, the Image Reduction and Analysis Facility, is distributed by the National Optical Astronomy Observatory, which is operated by the Association of Universities for Research in Astronomy under cooperative agreement with the National Science Foundation.

Table 1. Observation log

Field (1)	RA (2)	DEC (3)	Date (4)	Exposure (5)
1	00:42:47.6	+41:16:37.4	2014-10-03	3×1800 s
2	00:42:44.7	+41:16:07.6	2014-10-03	4×1200 s
3	00:42:49.5	+41:14:36.8	2014-10-03	3×1200 s
4	00:42:44.4	+41:16:07.7	2016-09-30	3×1200 s
5	00:42:44.1	+41:16:09.5	2016-09-30	3×1800 s
6	00:42:44.1	+41:16:08.2	2016-09-30	4×1200 s
7	00:42:44.2	+41:16:09.1	2016-09-30	3×1200 s
8	00:42:44.4	+41:16:07.7	2016-09-30	3×1200 s

Note. — (1): Each field has an independent set of targets.
(2)-(3): Field center, in epoch 2000; (4) UT date of observation;
(5) Exposure time in units of seconds.

with an average offset of 0.04 km s^{-1} and an root-mean-square (rms) of 13.1 km s^{-1} . Throughout this work, radial velocities have been corrected to heliocentric values.

3. Analysis and results

We analyze the Hydra spectra of the 77 HPNe and 300 MMDOs, focusing on the most prominent nebular emission lines. We first describe the procedure to fit the lines in Section 3.1, and then present the results of emission line diagnostics (Section 3.2) and kinematics (Section 3.3).

3.1. Emission line fitting

We begin with the MMDOs, the majority of which are located in the M31 disk and virtually unaffected by the strong stellar background emission. A typical MMDO spectrum is demonstrated in the top panel of Figure 3. Eight emission lines are clearly shown, including $\text{H}\beta$, $[\text{O III}] \lambda\lambda 4959, 5007$, $[\text{N II}] \lambda\lambda 6548, 6583$, $\text{H}\alpha$ and $[\text{S II}] \lambda\lambda 6716, 6731$. We fit the lines in the following steps.

First, we assume that each emission line has the Gaussian profile, and that any residual continuum after sky subtraction can be accounted for by a piecewise power-law in the vicinity of the lines. The Gaussian centroid of the line defines the radial velocity, and the observed width of the Gaussian profile is determined by the convolution of the intrinsic dispersion (σ_{PN}) and the instrumental broadening ($\sigma_{\text{inst}} \approx 1.41 \text{ \AA}$, or $\sim 84 \text{ km s}^{-1}$ at 5000 \AA). Second, we tie the radial velocities and σ_{PN} among $\text{H}\beta$, $\text{H}\alpha$ and $[\text{N II}] \lambda\lambda 6548, 6583$. Visual examination of the spectra indicates that this is reasonable for all cases. The parameters of the $[\text{S II}]$ doublet, which have relatively low signal-to-noise ratio (S/N), are also tied to those of $\text{H}\alpha$. $[\text{O III}] \lambda\lambda 4959, 5007$ are of higher ionization and might arise from regions with different physical conditions in the nebula; they are fitted with an independent radial velocity and σ_{PN} . Third, we tie the intensities of the $[\text{O III}]$ lines according to the theoretical ratio of $\lambda 4959/\lambda 5007 = 1:3$. The same ratio was assumed for the $[\text{N II}]$ doublet. In total, we have 10 free parameters for eight emission lines, plus several parameters for the power-law continuum, which are of less interest and will not be further discussed here.

In three cases, a single Gaussian profile provides a poor fit to the lines, in particular $[\text{O III}] \lambda 5007$ and $\text{H}\alpha$. Visual examination indicates that this is probably due to the presence of a second velocity component, as illustrated in Figure 4. Hence we add a second Gaussian component for such cases, linking its intrinsic dispersion to the primary component. The spectra are fitted using the IDL routine *mpfitexpr* (Bevington & Robinson 1992). The derived emission line intensities, radial velocities and intrinsic dispersions of the MMDOs are given in Table 2. Errors for these parameters are estimated using a bootstrapping method. We corrected the line intensities for the Galactic foreground extinction, using an average Galactic extinction curve and $E(\text{B-V})=0.062$ (Schlafly & Finkbeiner 2011).

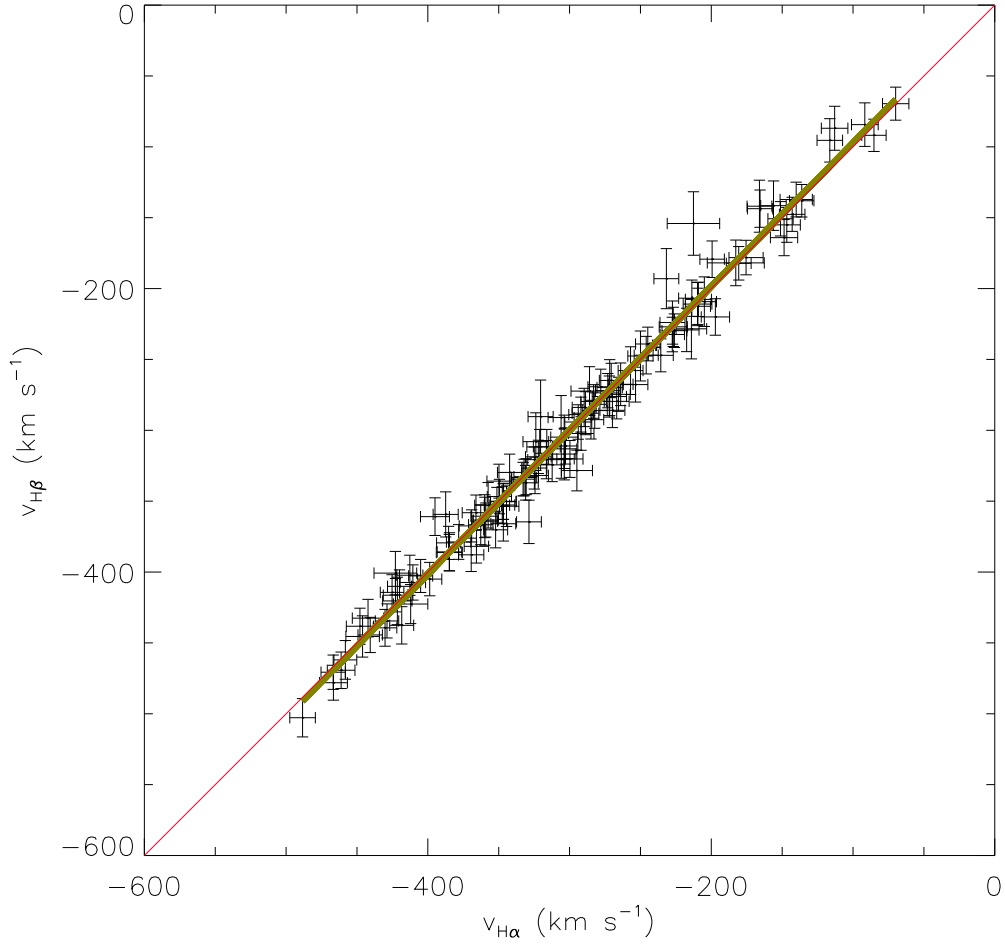


Fig. 2.— A comparison between the H α and H β radial velocities of MMDOs derived from our WIYN/Hydra dataset. The two lines are fitted independently with two Gaussian lines. Only objects with S/N>3 in both lines are included. The thin red diagonal line represents a 1:1 correspondence. The thick green line is the best linear-fit, which indicates no systematic offset between the two velocities and thus verifies the accuracy of our wavelength calibration.

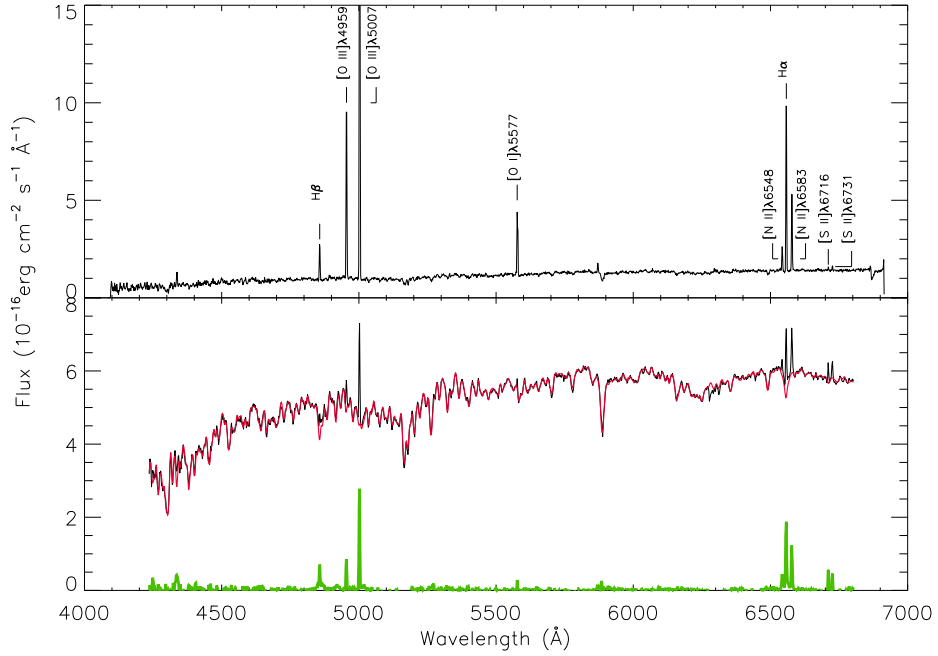


Fig. 3.— *Top panel:* A typical MMDO spectrum (MMDO 907), showing eight prominent emission lines: $H\beta$, $[O\ III]\ \lambda\lambda 4959, 5007$, $[N\ II]\ \lambda\lambda 6548, 6583$, $H\alpha$, and $[S\ II]\ \lambda\lambda 6716, 6731$. Note the residual $[O\ I]\ \lambda 5577$ sky emission line, which is not included in our analysis. *Bottom panel:* A typical Hydra spectrum of HPNe (#63) is shown as the black curve. The continuum is dominated by bulge stellar continuum emission falling in the fiber. Red curve is the best-fit stellar continuum using the pPXF+MILES synthetic library. The green curve shows the residual PN spectrum after stellar subtraction, where all eight emission lines remain.

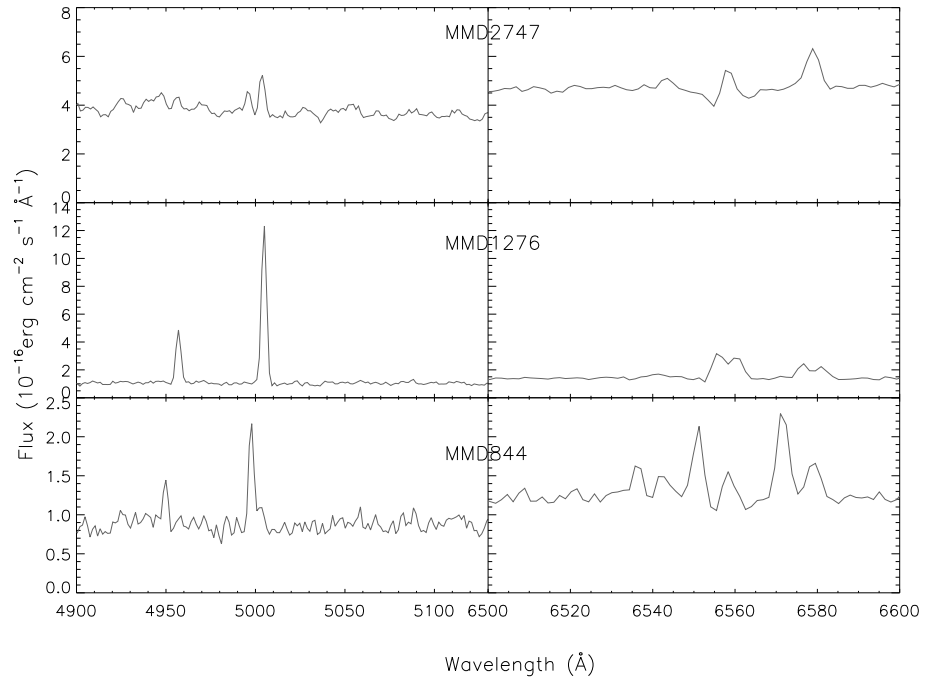


Fig. 4.— Three MMDOs exhibiting double-component emission lines. MMDO 844 has two components in [O III], [N II] and $\text{H}\alpha$. MMDO 1276 has double-peak in $\text{H}\alpha$ and [N II]. MMDO 2747 has a double-peak profile in [O III].

Table 2. Emission lines of MMDOs

Object (1)	RA (2)	DEC (3)	$v_{H\alpha}$ (4)	$v_{[OIII]}$ (5)	$\sigma_{H\alpha}$ (6)	$\sigma_{[OIII]}$ (7)	$F_{H\beta}$ (8)	$F_{[OIII]}$ (9)	$F_{H\alpha}$ (10)	$F_{[NII]}$ (11)	$F_{[SII]6716}$ (12)	$F_{[SII]6731}$ (13)
MMD1062	10.30333	41.22556	-556.± 1.3	-556.± 1.1	25.± 1.5	0.± 0.0	0.17±0.01	2.10±0.05	0.79±0.03	0.07±0.01	0.00±0.00	0.01±0.01
MMD1053	10.32167	41.26694	-441.± 1.3	-453.± 1.1	0.± 0.0	13.± 0.9	0.15±0.02	2.42±0.04	0.62±0.02	0.05±0.01	0.00±0.01	0.02±0.01
MMD1039	10.32292	41.20167	-370.± 0.4	-367.± 0.8	0.± 0.0	0.± 0.0	0.13±0.01	2.45±0.04	0.92±0.01	1.58±0.02	0.12±0.01	0.12±0.01
MMD2732	10.32333	41.31250	-404.± 7.8	-389.± 3.8	28.± 9.9	27.± 6.7	0.05±0.01	0.44±0.04	0.18±0.03	0.04±0.01	0.00±0.01	0.00±0.00
MMD1576	10.33292	41.13917	-433.± 0.2	-433.± 0.8	0.± 0.0	0.± 0.0	3.33±0.05	3.53±0.05	22.99±0.10	5.81±0.03	1.67±0.04	1.15±0.05
MMD1029	10.33625	41.17139	-296.± 0.8	-288.± 1.0	0.± 0.0	0.± 0.0	0.23±0.02	2.66±0.06	1.46±0.03	0.61±0.02	0.04±0.00	0.08±0.01
MMD784	10.34000	41.34500	-324.± 0.2	-323.± 0.8	0.± 0.0	0.± 0.0	2.90±0.07	4.08±0.06	12.60±0.08	2.99±0.03	1.09±0.02	0.74±0.02
MMD1051	10.34750	41.24111	-403.± 0.4	-397.± 0.6	0.± 0.0	0.± 0.0	0.65±0.02	12.50±0.11	4.91±0.05	1.55±0.02	0.04±0.01	0.12±0.01
MMD2787	10.37958	41.16000	-433.± 0.7	-427.± 0.7	0.± 0.0	0.± 0.0	0.34±0.02	5.08±0.06	1.20±0.03	1.04±0.02	0.06±0.01	0.08±0.02
MMD1044	10.39042	41.21556	-402.± 0.7	-403.± 0.8	0.± 0.0	0.± 0.0	0.27±0.02	5.43±0.09	1.68±0.04	0.73±0.02	0.06±0.02	0.00±0.00

Note. — (1) name of MMDOs, numbered as in Merrett et al. (2006); (2)-(3) Sky coordinates, in Epoch 2000; (4) Heliocentric radial velocity of the $H\alpha$ emission line, in units of km s^{-1} ; (5) Heliocentric radial velocity of $[O III]\lambda 4959,5007$, in units of km s^{-1} ; (6) Intrinsic velocity dispersion of $H\alpha$, in units of km s^{-1} ; (7) Intrinsic velocity dispersion of $[O III]\lambda 4959,5007$, in units of km s^{-1} . Values of zero in column (6)-(7) indicate objects whose emission lines appear narrower than the instrument broadening. (8)-(13) Fluxes of the emission lines, in units of $10^{-15} \text{ erg s}^{-1} \text{ cm}^{-2}$. For three objects exhibiting double velocity components, the velocities and fluxes of both components are reported. Only a portion of the full table is shown here to illustrate its form and content. The full table will be published online.

The situation for the HPNe is more complicated, due to contamination from the stellar bulge and the existence of diffuse ionized gas in the bulge (Jacoby et al. 1985; Ciardullo et al. 1988). The spectra of our target PNe are dominated by the continuum emission of bulge stars, as shown in an example spectrum in the bottom panel of Figure 3. Therefore, we employ the Penalized Pixel-Fitting (pPXF; Cappellari & Emsellem 2004; Cappellari 2017) package to fit and subtract the stellar continuum. For the synthetic stellar template, we adopt the MILES library (Falcón-Barroso et al. 2011). pPXF decomposes the fitted spectrum into simple stellar populations (SSPs) with different ages and metallicities. A byproduct of the fit is the integrated stellar velocity field, in particular the line-of-sight velocity (V_*) and velocity dispersion (σ_*). By design, pPXF masks out the narrow wavelength ranges around the potential emission lines, e.g., $H\alpha$. The Balmer emission lines, especially $H\beta$, of the PNe would be affected by the Balmer absorption lines present in most SSPs. The forbidden lines, on the other hand, are free of this problem. We proceed with this caveat in mind and further address the potential effect in Section 3.2.

Since the current wavelength range (4119–6882 Å) does not cover the Balmer break at 3646 Å (Kauffmann et al. 2003) or the Ca II K and H lines (Wilson & Woolley 1970), our spectra are insensitive to the intermediate-age ($\lesssim 1$ Gyr) SSPs, which generally exhibit strong Balmer absorption lines. Fortunately, such intermediate-age SSPs, if any, are unlikely to be substantial in the M31 bulge (Saglia et al. 2010; Dong et al. 2015). Therefore, we select a subset of the MILES library to fit the spectra, which include SSPs with ages from 1 to 14.125 Gyr and metallicity $Z=0.008$ – 0.033 . This choice is warranted by our analysis of the stellar populations based on a CAHA/PPAK integral-field spectroscopic mapping of the M31 bulge (R. García-Benito et al. 2018, in preparation), which cover the Ca II K and H lines as well as the Balmer break. The hence fitted SSPs are predominantly old and are of 1–1.5 solar metallicity, which is consistent with the finding of Saglia et al. (2010) based on the long-slit spectra. It is noteworthy that the enclosed stellar mass within each $2''$ -diameter fiber is estimated to be 10^5 – $10^6 M_\odot$, based on the projected stellar mass distribution derived in Dong et al. (2015), and thus stochastic fluctuation due to a few bright stars in the modeled SSPs is negligible. An example of the modeled stellar continuum is shown by a red curve in the bottom panel of Figure 3.

After subtraction of the modeled stellar continuum, we employ the same approach as for the MMDOs to fit the emission lines, which should predominantly arise from the HPNe, although the presence of diffuse ionized gas might cause some contamination, due to the limitation of our multi-fiber observations (Section 2.2). We assess the degree of contamination from the diffuse ionized gas using our *HST* WFC3 narrow-band images (Figure 1; Z. Li et al. in preparation; see also Dong et al. 2014, 2016). It can be seen from Figure 1 that the majority of the HPNe are located outside the so-called *nuclear spiral* (Jacoby et al. 1985), where the diffuse ionized gas is concentrated. Using the [O III] image and taking into account the sky area covered by the fibers, we find that, in 52 out of the 77 HPNe, the diffuse ionised gas contributes less than 20% (and typically less than 10%) of the measured [O III] flux. This number drops to 51 HPNe, if we required that the contamination is less than 20% in all three lines of [O III], $H\alpha$, and [N II]. We restrict the following

statistical analysis to this subsample of 51 HPNe.

It turns out that all 77 HPNe exhibit the [O III] $\lambda 5007$ line with $S/N > 5$, confirming that they are genuine [O III]-emitting objects. We also find that a second velocity component is required for three objects (#21, #45 and #52), which exhibit double peaks in [O III], and a fourth object (#50) with double components in both [N II] and $H\alpha$. The fit results for the 77 HPNe, including line intensity, radial velocity and intrinsic dispersion, are given in Table 3.

Table 3. Emission lines of HPNe

Object (1)	RA (2)	DEC (3)	$v_{H\alpha}$ (4)	$v_{[OIII]}$ (5)	$\sigma_{H\alpha}$ (6)	$\sigma_{[OIII]}$ (7)	$F_{H\beta}$ (8)	$F_{[OIII]}$ (9)	$F_{H\alpha}$ (10)	$F_{[NII]}$ (11)	$F_{[SII]6716}$ (12)	$F_{[SII]6731}$ (13)
HPN1	10.64692	41.26445	-546.± 5.8	-519.± 15.0	96.± 8.4	75.± 16.0	0.40±0.04	0.35±0.05	0.63±0.05	0.37±0.07	0.07±0.02	0.08±0.02
HPN2	10.65542	41.27444	-333.± 3.8	-323.± 11.0	55.± 5.7	82.± 8.0	0.56±0.07	1.24±0.11	1.58±0.11	1.28±0.09	0.80±0.07	0.58±0.07
HPN3	10.65592	41.26389	-177.± 3.6	-178.± 1.2	75.± 7.3	38.± 9.8	1.99±0.12	14.47±0.83	3.04±0.22	0.21±0.07	0.02±0.06	0.06±0.07
HPN4	10.65750	41.26333	-366.± 8.8	-406.± 19.5	56.± 27.2	75.± 25.8	0.31±0.07	0.52±0.10	0.87±0.21	0.54±0.14	0.09±0.05	0.15±0.05
HPN5	10.65846	41.26694	-381.± 10.2	-177.± 31.8	62.± 19.4	175.± 25.6	0.69±0.11	1.64±0.29	0.83±0.17	1.30±0.25	0.70±0.11	0.60±0.11
HPN6	10.65963	41.25917	-374.± 4.2	-383.± 1.3	62.± 10.1	57.± 7.0	0.98±0.10	6.91±0.35	2.91±0.27	0.54±0.11	0.21±0.08	0.18±0.07
HPN7	10.66258	41.26305	-398.± 18.9	-320.± 29.3	64.± 26.1	142.± 38.1	0.23±0.06	0.57±0.14	0.31±0.10	0.35±0.10	0.14±0.06	0.10±0.06
HPN8	10.66271	41.27667	-286.± 8.1	-266.± 6.3	91.± 16.6	68.± 34.0	0.73±0.09	1.58±0.38	1.44±0.20	1.13±0.16	0.45±0.08	0.28±0.06
HPN9	10.66308	41.27611	-377.± 9.1	-382.± 10.3	74.± 18.1	89.± 16.3	0.48±0.07	0.96±0.12	0.67±0.12	0.62±0.12	0.21±0.07	0.18±0.06

Note. — (1) Name of HPNe; (2)-(13) The same as in Table 2. Only a portion of the full table is shown here to illustrate its form and content. The full table will be published online.

3.2. Line intensity diagnostics

In this section we focus on the four brightest lines: $H\beta$, $[\text{O III}] \lambda 5007$, $H\alpha$, and $[\text{N II}] \lambda 6583$. Figure 5 displays the line flux ratio of $R = \frac{[\text{O III}]}{H\alpha + [\text{N II}]}$ vs. $M_{\lambda 5007}$ for the 77 PNe. Herrmann et al. (2008) and Ciardullo (2010) have shown that this diagram can be used to exclude contaminations in PNe identification. Specifically, genuine PNe satisfy the relation $4 > \log R > -0.37 \times M_{\lambda 5007} - 1.16$. As shown in Figure 5, most of the HPNe meet this criteria, and it is also noteworthy that the overall distribution of HPNe in this diagram resembles that of the PNe from the literature, which also suggests that our targets are genuine PNe.

We also construct a BPT diagram (Baldwin et al. 1981) for the 77 HPNe and 300 MMDOs, as shown in Figure 6. Following Sanders et al. (2012), we adopt an empirical curve to distinguish the H II regions and PNe in this diagram. All of HPNe (green diamonds) lie in the expected PN region. The majority of the MMD PNe are also located in this region. However, 23 outliers might be actually H II regions, which needs further assessment.

No extinction was made when we measured these line ratios. However, this is unlikely to affect the above line ratios, given the close wavelengths of the two emission lines in each ratio. On the other hand, as stated in Section 3.1, the measured values of $H\beta$ in the HPNe might be biased too high, due to degeneracy with the $H\beta$ absorption line as predicted by the modeled stellar spectra. To correct for this potential bias in $H\beta$, we have set an upper-limit to the flux of $H\beta$ based on $H\alpha$. Bright bulge PNe (which is the case for HPNe) generally have circumstellar extinction of around $A_{\lambda 5007} \sim 0.8$ (Richer et al. 1999; Jacoby & Ciardullo 1999), and the inner bulge of M31 has been found to have low local extinction (Dong et al. 2016). Thus by assuming the Case B theoretical ratio $H\alpha/H\beta = 2.85$ (Storey & Hummer 1995), we estimate that $I(H\alpha)/3.45 = I(H\beta)$. This can be used as an upper-limit flux of $H\beta$ for the HPNe with initial $H\alpha/H\beta < 3.45$. We verify that the $H\beta$ intensity after extinction correction does not show any artificial radial trend.

The $[\text{N II}] \lambda 6583/H\alpha$ and $[\text{O III}] \lambda 5007/H\beta$ intensity ratios as a function of the projected galactocentric radius R are shown in Figure 7, for the 51 HPNe in which contamination from diffuse emission is negligible (Section 3.1). In each panel, only those objects (HPNe or MMDOs) with an $S/N > 3$ in the four lines are included. To see the trend of these ratios versus R , we also plotted the line ratios of M31 outer-disk and halo PNe retrieved from the literature (Kwitter et al. 2012; Balick et al. 2013; Corradi et al. 2015; Fang et al. 2013, 2015a, 2018). The $[\text{O III}]/H\beta$ ratios of our sample show larger dispersion, especially for the HPNe. The HPNe, located exclusively at $R < 0.5$ kpc, show on average higher $[\text{N II}]/H\alpha$ and lower $[\text{O III}]/H\beta$ (Figure 7), compared to the MMDOs, which mostly reside at $0.5 < R < 4$ kpc. The PNe in the outer-disk and halo of M31 generally have lower $[\text{N II}] \lambda 6583/H\alpha$ ratios than our sample of the HPNe but comparable $[\text{O III}] \lambda 5007/H\beta$ ratios.

The higher $[\text{N II}]/H\alpha$ of HPNe can be naturally understood as the result of an on-average higher stellar nitrogen abundance in the inner bulge, compared to the disk (Saglia et al. 2010; Sanders et al. 2012). The decreasing trend in $[\text{O III}]/H\beta$ can also be understood as a higher

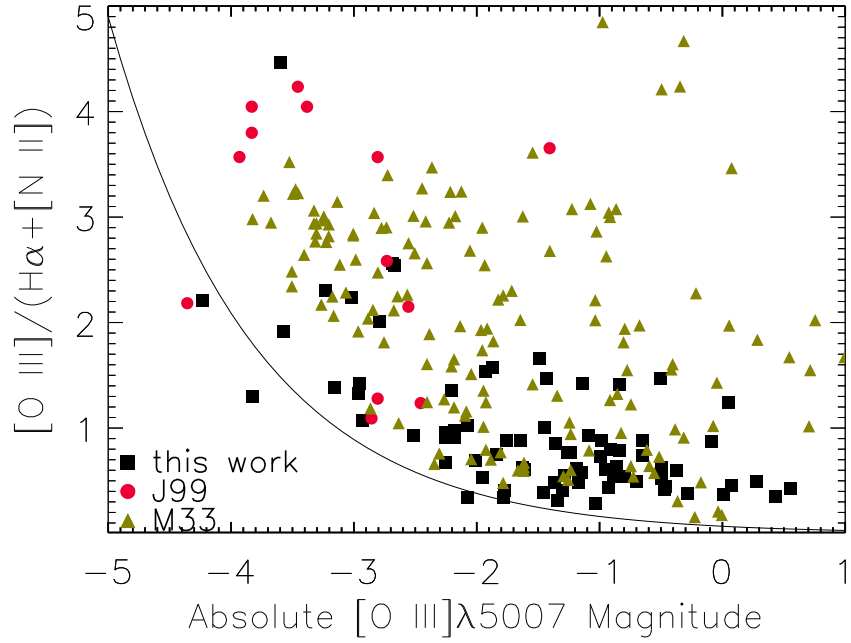


Fig. 5.— The $[O\ III]\lambda 5007 / (H\alpha + [N\ II])$ ratio versus the $[O\ III]\lambda 5007$ absolute magnitude. Black squares: HPNe in this work; Red circles: PNe in M31's bulge (Jacoby & Ciardullo 1999); Green triangles: PNe in M33 (Ciardullo et al. 2004). Black curve is the relation between the two quantities, in the form of $\log X = -0.37 \times Y - 1.14$ (see text for explanation).

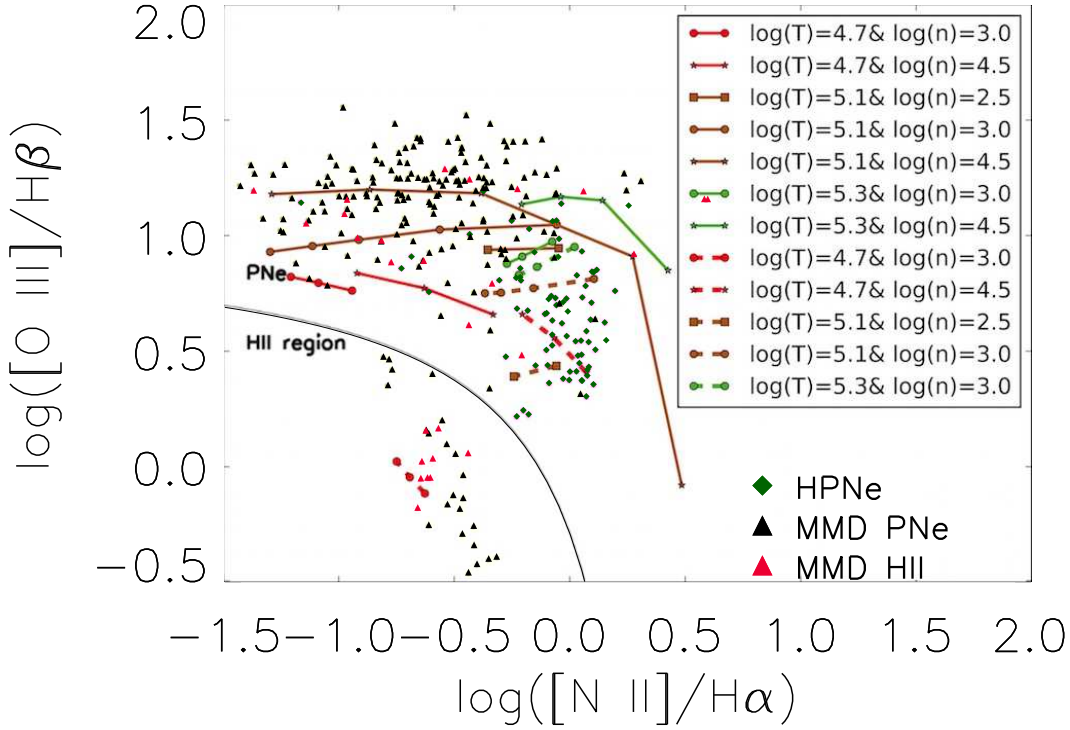


Fig. 6.— A BPT diagram for HPNe and MMDOs. Green diamonds: HPNe candidates; Black triangles: MMD PNe candidates; Red triangles: MMD HII region candidates. For the few objects with double-peak emission lines, the line flux is the sum of the two components. The black curve shows an empirical division of PNe and HII regions (Sanders et al. 2012). Squares, circles, stars, and triangles linked by solid or dashed lines represent the 3MdB photoionization models (Morisset et al. 2015) of the same effective temperature (T , in units of K) and column density (n , in units of cm^{-3}), but of different luminosities of the central star. Solid lines are for models of near-solar abundance ($12 + \log[\text{O}/\text{H}] = 8.64$), mass-bounded model, while dashed lines are for “very high” abundance ($12 + \log[\text{O}/\text{H}] = 9.24$), radiation-bounded model.

oxygen abundance, which in a photoionized gas would lead to a lower electron temperature and consequently a lower value of $[\text{O III}]/\text{H}\beta$ (Nagao et al. 2006). To further understand the occupation of HPNe in the BPT diagram, we explore the Mexican Million Models database (3MdB; Morisset et al. 2015), which is a large set of numerical simulations for photoionized clouds (including PNe), based on CLOUDY (Ferland et al. 1998). We plot in Figure 6 model-predicted line ratios from the most relevant 3MdB PN models, with a variety of gas density and effective temperature of the central star, as well as metallicity. Apparently, the observed line ratios of both the HPNe and MMD PNe can be reproduced by the chosen models. In particular, the HPNe can be matched by models with a super-solar metallicity, while the MMD PNe can be matched by models with a near-solar metallicity. This further supports a connection between the observed line ratio gradients and the metal-enriched bulge of M 31.

3.3. Kinematics

For each object, we measured two radial velocities, one related to $\text{H}\alpha$ and the other related to $[\text{O III}] \lambda 5007$. Our measurements of the $[\text{O III}]$ velocities (only for the MMDOs) are compared with those derived by MMD06 in Figure 8-(a), and excellent agreement is seen. As for the 77 HPNe, 29 have at least one $[\text{O III}]$ velocity measurement in previous studies, of which 26 were reported by MMD06, 10 by Halliday et al. (2006), 2 by Sanders et al. (2012), and another 2 by Pastorello et al. (2013). A comparison with these measurements is shown in Figure 8-(b). While reasonable agreement is found for most objects, in several cases obvious difference still exists.

We suggest that our results should be more robust, due to our deeper exposures and extra use of the $[\text{O III}] \lambda 4959$ nebular line. It is noteworthy that the PNe with a second velocity component in $[\text{O III}]$ or $\text{H}\alpha$ (Section 3.1) generally have one component consistent with previous measurements. The two components in the velocity have separations of $\gtrsim 200 \text{ km s}^{-1}$. This might signify fast bipolar outflows in PNe, which are highly inclined with respect to the line of sight. Bipolar outflows with expansion velocities as fast as 300 km s^{-1} have been detected in the Milky Way PNe (e.g., Fang et al. 2015b; Danehkar et al. 2016). The origin of such fast outflows remains elusive, but this topic is beyond the scope of discussion of this work.

We also check the distribution of the difference between the $[\text{O III}]$ and $\text{H}\alpha$ velocities, $V_{\lambda 5007} - V_{\text{H}\alpha}$, of the two groups (HPNe and MMDOs), as shown in Figure 9. For the MMDOs, there is no obvious systematic offset between $V_{\lambda 5007}$ and $V_{\text{H}\alpha}$, although the maximum difference approaches $\pm 200 \text{ km s}^{-1}$. The HPNe show a somewhat larger scatter in this difference. For the HPNe, there is an extended distribution of the velocity difference in the range -160 to -100 km s^{-1} , but this asymmetry is statistically insignificant (only $\sim 2\sigma$). $[\text{O III}]$ requires higher excitation, so its location in PNe and expansion velocity may be different from other emission lines. Unless otherwise specified, in the discussion hereafter, we use the line-of-sight velocity measured from $\text{H}\alpha$, whose emission distribution in PNe is more homogeneous than $[\text{O III}]$ and thus is expected to be more representative, to carry out the kinematic and dynamical analysis.

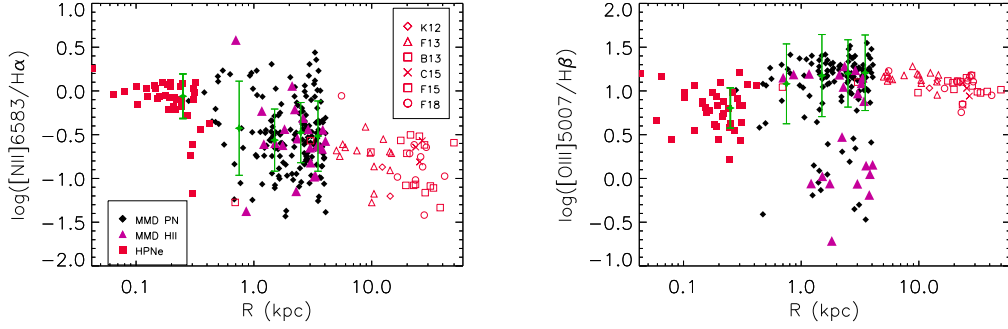


Fig. 7.— $[\text{N II}]\lambda 6583/\text{H}\alpha$ (left) and $[\text{O III}]\lambda 5007/\text{H}\beta$ (right) intensity ratios as a function of projected galactocentric radius. In both panels, black diamonds represent the MMD PNe, purple triangles are the MMD H II regions, and red squares are the 51 HPNe in which contamination from diffuse emission is negligible (Section 3.1). Only objects with $\text{S/N} > 3$ in these four emission lines are included. HPNe and the MMD PNe are grouped by projected radii in 0–0.5, 0.5–1, 1–2, 2–3 and 3–4 kpc; green dots are the median values of these five regions along with the 68% quantile bar. Red open symbols are the M31 outer-disk and halo PNe retrieved from the literature (see text for description).

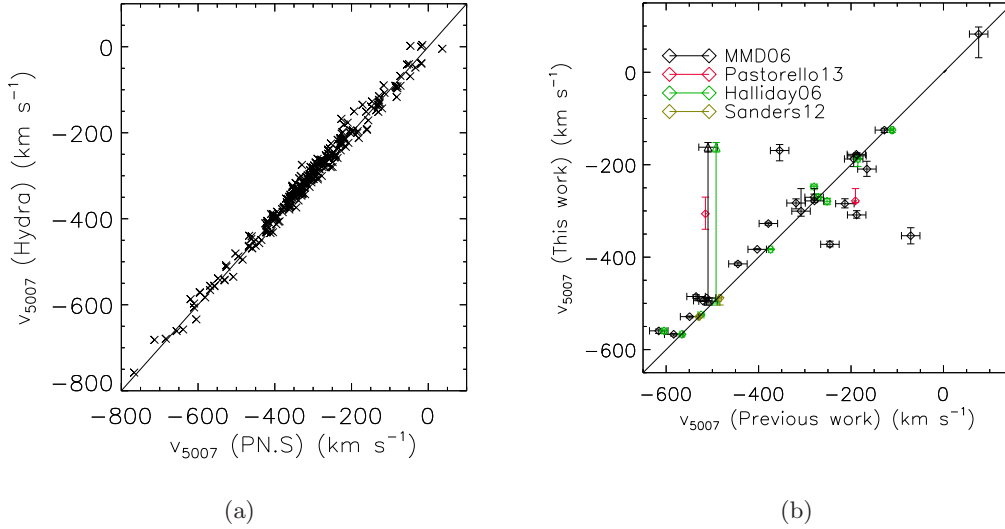


Fig. 8.— Comparison of $[\text{O III}]\lambda 5007$ radial velocities measured from this work and from previous work. Left: MMDOs; Right: HPNe. In the right panel, the black or green lines linking two triangles stand for the HPNe with double components in $[\text{O III}]\lambda 5007$ found in this work. In both panels, the black diagonal line represents a 1:1 correspondence.

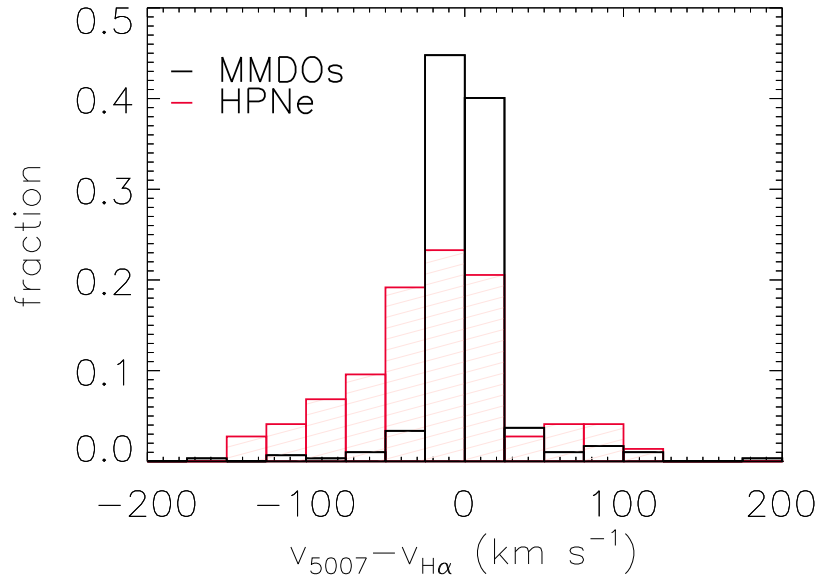


Fig. 9.— Histograms of the difference between the radial velocities derived from [O III] and H α .

After correcting for M31’s systemic (heliocentric) velocity of -301 km s^{-1} (de Vaucouleurs et al. 1991), the radial velocities $V_{\text{H}\alpha}$ of HPNe range from -245 km s^{-1} to 283 km s^{-1} ; 90% of them lie within $\pm 166 \text{ km s}^{-1}$. This is compatible with the bulge velocity dispersion of $\sim 166 \text{ km s}^{-1}$ (Saglia et al. 2010), which is a corroborative support to our presumption that all our HPNe reside in M31’s bulge. On the other hand, the MMDO objects have radial velocities between -374 km s^{-1} and 319 km s^{-1} , which is compatible with the maximum circular velocity ($\sim 250 \text{ km s}^{-1}$; Braun 1991) of the M31 disk.

Given that the velocity ranges of these two groups of PNe are consistent with the literature, we expect that their radial velocity distributions are also consistent with the intrinsic rotation pattern of M31 (here we assume a clockwise rotation of M31 as observed from the top of the disk). The spatial distribution of radial velocities in M31 disk is visually illustrated in Figure 10, where HPNe and MMDOs with the red-shifted and blue-shifted velocities (with respect to the systemic velocity of M31) are displayed separately. The radial velocity map is supposed to be symmetric about the minor axes of the disk where the signs of the radial velocities of the PNe distributed in the north and south regions are opposite.

Indeed, the MMDOs show the radial velocities approximately symmetric about the minor-axis of the disk (with a position angle of $\sim 128^\circ$, east of south; Kent 1989): $79 \pm 10\%$ of the MMDOs in the northeastern disk region are red-shifted, while $88 \pm 11\%$ in the southwestern disk region are blue-shifted. Interestingly, the HPNe display a similar rotation pattern: $97_{-25}^{+3}\%$ of the HPNe in the northeast region are red-shifted; $90_{-24}^{+10}\%$ of the HPNe in the southwest region are blue-shifted. We further test this pattern by considering the position angle of the bulge kinematic minor axis (PA_k) as a free parameter, which is derived by maximizing the sum of $\sum_i [V_i \cos(\text{PA}_i - \text{PA}_k)]$, where V_i and PA_i are the radial velocity and position angle of the i th HPNe, respectively. This results in $\text{PA}_k = 130^\circ \pm 4.1^\circ$. PA_k can also be estimated using the line-of-sight velocity of the integrated stellar continuum at the position of each HPN, as derived from our pPXF fits (Section 3.1). This leads to $\text{PA}_K = 125^\circ \pm 9.2^\circ$. Both values of PA_K are consistent, within the errors, with the position angle of the disk minor-axis.

Therefore, both discrete tracers (i.e., the HPNe) and the integrated starlight show significant rotation in the inner bulge of M31, as previously found by Saglia et al. (2010) through long-slit spectroscopy. Nevertheless, Saglia et al. (2010) argued that the M31 bulge is a slow rotator, which has an intensity-weighted mean $V/\sigma \approx 0.2$. We also calculate an intensity-weighted average of V/σ , using V_* and σ_* measured at the position of each HPNe; here the intensity refers to the median of the underlying stellar continuum in $5000\text{--}5500\text{\AA}$. A similar value of $V/\sigma \approx 0.20$ is found, which confirms that the inner bulge of M31 is a slow rotator.

Lastly, we examine the distribution of the intrinsic dispersion of the [O III] line, σ_{5007} , as shown in Figure 11. Due to the moderate spectral resolution ($\sigma_{\text{inst}} \approx 84 \text{ km s}^{-1}$) and typical PN expansion velocities of $\lesssim 30 \text{ km s}^{-1}$, the observed lines are not expected to be resolved. This is indeed the case for $\sim 82\%$ of the MMDOs, which have σ_{5007} consistent with zero. On the other

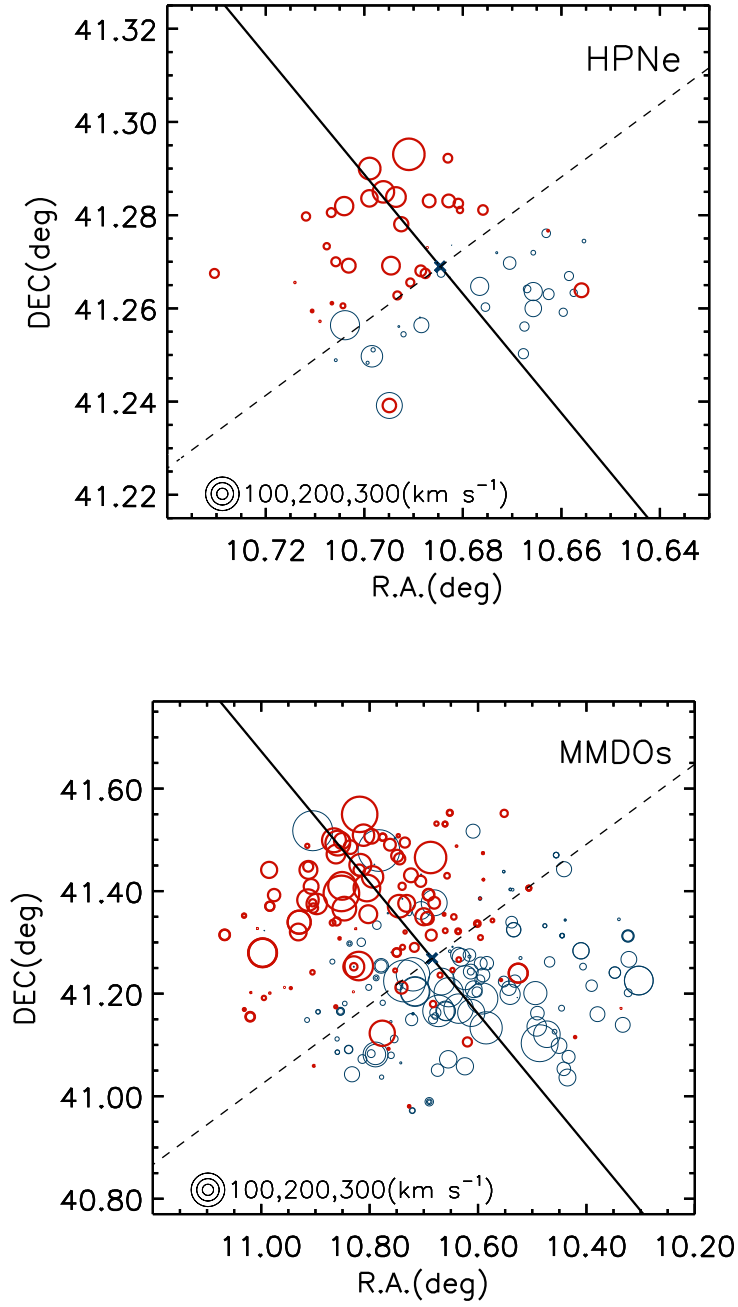


Fig. 10.— Radial velocity (corrected for the systemic velocity of M31) map of the spectroscopically confirmed HPNe (top) and MMO PNe (bottom). Red and blue circles represent red- and blue-shifted objects, respectively, with the circle size proportional to the absolute velocity. The solid and dashed lines indicate the major- and minor-axis of M31, respectively. A rotation pattern about the minor-axis is evident in both panels.

hand, $\sim 54\%$ of the HPNe exhibit σ_{5007} greater than 70 km s^{-1} . To see whether the bulge diffuse emission might have affected the measurement, we also plot in Figure 11 a subset of 18 HPNe (green histogram), whose $[\text{O III}]\lambda 5007$ line is detected with an $\text{S/N} \geq 10$, ensuring a robust measurement for the dispersion. This subset also shows a significant fraction of large σ_{5007} , suggesting that this is an intrinsic property. We address the possible physical cause of such high dispersions in Section 4.2.

4. Discussion

4.1. Genuine circumnuclear PNe

The above spectral analysis confirms that the 77 PN candidates selected from the *HST* image are genuine emission line objects in the circumnuclear region of M31. The relationship given in Herrmann et al. (2008) (Figure 5) and the BPT diagram (Figure 6) further suggests that the majority of them are consistent with the PN nature, rather than compact H II regions. Moreover, the circumnuclear region of M31 is known to be free of recent or on-going star formation (Rosenfield et al. 2012; Dong et al. 2015), hence no contamination from young, massive stars is expected. There might be, however, other types of emission line objects that could mimic the observed spectra of PNe.

In particular, symbiotic stars are often considered as a major source of confusion (Boissay et al. 2012). In our Galaxy, about 1200 symbiotic star candidates have been found in $\text{H}\alpha$ photometric survey, however, only ~ 300 are confirmed to be genuine symbiotic stars through spectroscopy (Miszalski et al. 2013), which is much lower than the number of confirmed Galactic PNe (~ 3500 , Parker et al. 2016). This may suggest a negligible, if any, contamination by symbiotic stars in our sample, unless the actual occurrence rate of symbiotic stars in M31’s bulge is much different from that in our Galaxy, which is unlikely. Another contamination might come from the so-called super-soft X-ray sources (SSSs), generally thought to be white dwarfs stably accreting from a low-mass companion (Di Stefano et al. 1995). Ten SSSs have been reported in the bulge of M31, based on the *Chandra* observations (Di Stefano et al. 2004), but none of them coincides with our HPNe in spatial location. Another source of possible contamination might be young, which is compact supernova remnants (SNRs). However, no remnants of core-collapsed SNe are expected in M31’s bulge, again due to the lack of recent star formation; remnants of Type Ia SNR might be present, but their number is expected to be small at any given time. Currently only three SNRs are known in the inner bulge of M31 (Kong et al. 2003). We thus conclude that the 77 PN candidates are most likely genuine PNe.

4.2. Environmental effect on the circumnuclear PNe?

Figure 11 indicates that most MMD PNe show value of σ_{5007} quite consistent with typical PN velocity dispersions of 10–30 km s⁻¹ (Kwok 2000), whereas a substantial fraction of HPNe exhibit large values of σ_{5007} up to ~ 100 km s⁻¹. This difference is unlikely due to different populations of progenitor/central stars. Instead, we speculate that environmental effects might have caused the difference. In particular, the bulge of M31 is known to be filled with a corona of diffuse hot gas (Li & Wang 2007; Li et al. 2009). Materials ejected by stars randomly orbiting in the bulge (or in elliptical galaxies), including stellar winds and PN shells, would inevitably be shock-heated by the hot gas and subsequently become part of the latter, a process fundamental to the cycling and metal-enrichment of the interstellar medium (Mathews 1990). Details of this process were modeled by Bregman & Parriott (2009), who simulated the interaction of the expanding PN shell with the ambient hot gas of varied temperatures and densities, during which the hot flow transports both heat and momentum to the nebula. According to their simulations, part of the nebula can be accelerated to about half of the progenitor star’s orbiting velocity (represented by the bulge velocity dispersion). Observationally, however, the interaction between a PN and the ambient hot gas has rarely been caught in real time. The large σ_{5007} seen in some of the HPNe might be providing an indirect evidence for the shock-heated and accelerated shell materials, although this has to be further verified by a self-consistent model suitable for the M31 bulge.

4.3. Dynamical Mass of the inner bulge

At present, while there has been ample evidence for the existence of dark matter (DM) in the outer regions of large disk galaxies such as M31, the amount and distribution of DM in the central region is poorly known. In the case of M31, the baryonic mass budget in the central ~ 500 pc region, as reviewed by Li et al. (2009), is relatively well determined and overwhelmingly dominated by the stars. The kinematic tracers like PNe has the great potential to tightly constrain the mass and even the spatial distribution of DM in the central region of a massive galaxy, given a robust measurement of the total dynamical mass.

The radial velocities of our HPNe can provide a useful estimate of the dynamical mass. We adopt the projected mass estimator proposed by Heisler et al. (1985), $GM = f/N \times \sum_i V_i R_i$, where V_i is the PN radial velocity (from H α), R_i is the projected galactocentric radius, G is the gravitational constant, N is the total number of tracer particles, and $f=10.2$ is a scaling parameter depending on the distribution of orbits (Heisler et al. 1985). We restrict the analysis on 38 HPNe located within 70'' (~ 267 pc), i.e., the largest radius that fits the *HST* field-of-view (the cyan circle in Figure 1). Strictly speaking, this estimator should be applied to the tracers of an isotropic velocity distribution, which is a reasonably approximation in the inner bulge of M31, which again shows only moderate rotation (see the analysis in Section 3.3).

We thus estimate an enclosed mass of $5.9 \pm 0.4 \times 10^9 M_\odot$ within an effective (de-projected) radius

of 340 pc (as corrected from the projected 267 pc by a factor of $4/\pi$). The error is estimated using a bootstrapping method. As explained in Section 3.3, this calculation is based on the $H\alpha$ velocities. In order to estimate the systematic error introduced by this method, we also use the $[O\ III]$ velocities and obtained an enclosed mass of $6.9\pm 0.6\times 10^9 M_{\odot}$. These two masses are consistent with each other within the errors.

We contrast the estimate dynamical mass with the latest mass models of M31 in the literature. Combining the SDSS *ugriz* photometry and the *Spitzer* $3.6\mu\text{m}$ imaging, Tamm et al. (2012) performed SED fitting to derive the parameterized 3-dimensional stellar mass distribution of M31. They accounted for the additional baryonic components, in particular the H I disk, which provides strong constraints on the total gravitational mass at large radii. This in turn allowed them to parameterized the DM distribution, following either an NFW profile, a Moore profile, or an Einasto profile. In the central 340 pc of M31, the total mass is dominated by the stellar mass, which, according to the model of Tamm et al. (2012), has a value of $3.7\times 10^9 M_{\odot}$; however, a higher value of $5.6\times 10^9 M_{\odot}$ was also permitted, as not to violate the maximally allowed stellar mass at large radii. The latter value is very close to our estimated dynamical mass, leaving little room for the DM; while adopting the former value would indicate a perhaps unrealistically high amount of the DM. We note that the stellar mass estimate of Tamm et al. (2012) was based on a Charier initial mass function (IMF), which, as they found, is preferred by the mass budget in the disk. Adopting a steeper IMF for the inner bulge could substantially raise the stellar mass. We conclude that at present the largest uncertainty in determining the DM mass in the inner bulge of M31 probably lies in the uncertainty in the stellar IMF.

5. Summary

Using the WIYN/Hydra multi-object spectrograph, we have obtained fiber spectra for 77 PN candidates in the circumnuclear region of M31. The majority (64%) of this sample are observed for the first time in the spectroscopy. These spectra are analyzed and results discussed in terms of their PN nature, kinematics and dynamics. We have also obtained spectra of 300 emission line objects (PNe and H II regions) that were identified in previous surveys; most of these objects primarily reside in the M31 disk. Our main results are as follows:

- All 77 circumnuclear PN candidates are genuine emission line objects, most probably PNe.
- Combining our circumnuclear PNe and the disk sample from previous observations, the intensity ratio of $[N\ II]\lambda 6583/H\alpha$ generally shows a trend of decrease with the galactocentric radius, while the $[O\ III]\lambda 5007/H\beta$ ratio is generally flat, and large scatter exist in the disk sample.
- The radial velocities of the circumnuclear PNe reveal the rotation of the inner bulge, which is consistent with the pattern of kinematics about the minor-axis of M31’s disk.

- From the radial velocities of our sample, we estimate a dynamical mass of $6.4 \pm 0.5 \times 10^9 M_{\odot}$ for the bulge region enclosed within an effective radius of 340 pc.

We emphasize that this is the first effort that combines the *HST* narrow-band images and follow-up spectroscopy on a ground-based telescope, to identify PN candidates in the inner bulge of M31, where the stellar background emission is so strong that clean removal of such contamination is extremely difficult. In the near future, it is highly desired to extend the spectroscopic study on the remaining, albeit on average fainter, circumnuclear PN candidates in M31.

This work is supported by the National Key Research and Development Program of China (No. 2017YFA0402703) and National Science Foundation of China under grant 11133001. We thank the referee for helpful comments. A.L. and Z.L. are grateful to Eric Hooper and Diane Harmer of the WIYN Observatory for their help with the Hydra observations. Z.L. acknowledges support from the Recruitment Program of Global Youth Experts. H.D. acknowledges funding support from the European Research Council under the European Union’s Seventh Framework Programme (FP7/2007-2013)/ERC grant agreement n^o[614922].

REFERENCES

- Baldwin, J. A., Phillips, M. M., & Terlevich, R. 1981, *PASP*, 93, 5
- Balick, B., Kwitter, K. B., Corradi, R. L. M., & Henry, R. B. C. 2013, *ApJ*, 774, 3
- Barden, S. C., & Armandroff, T. 1995, in *Proc. SPIE*, Vol. 2476, *Fiber Optics in Astronomical Applications*, ed. S. C. Barden, 56–67
- Bevington, P. R., & Robinson, D. K. 1992
- Boissay, R., Parker, Q. A., Frew, D. J., & Bojicic, I. 2012, 283, 316
- Braun, R. 1991, *ApJ*, 372, 54
- Bregman, J. N., & Parriott, J. R. 2009, *ApJ*, 699, 923
- Cappellari, M. 2017, *MNRAS*, 466, 798
- Cappellari, M., & Emsellem, E. 2004, *PASP*, 116, 138
- Ciardullo, R. 2010, *PASA*, 27, 149
- Ciardullo, R., Durrell, P. R., Laychak, M. B., et al. 2004, *ApJ*, 614, 167
- Ciardullo, R., Jacoby, G. H., Ford, H. C., & Neill, J. D. 1989, *ApJ*, 339, 53

- Ciardullo, R., Rubin, V. C., Ford, Jr., W. K., Jacoby, G. H., & Ford, H. C. 1988, *AJ*, 95, 438
- Coccatto, L., Gerhard, O., Arnaboldi, M., et al. 2009, *MNRAS*, 394, 1249
- Corradi, R. L. M., Kwitter, K. B., Balick, B., Henry, R. B. C., & Hensley, K. 2015, *ApJ*, 807, 181
- Danehkar, A., Parker, Q. A., & Steffen, W. 2016, *AJ*, 151, 38
- de Vaucouleurs, G., de Vaucouleurs, A., Corwin, Jr., H. G., et al. 1991
- Delgado-Inglada, G. 2016, *ArXiv e-prints*, arXiv:1611.10246
- Di Stefano, R., Paerels, F., & Rappaport, S. 1995, *ApJ*, 450, 705
- Di Stefano, R., Kong, A. K. H., Greiner, J., et al. 2004, *ApJ*, 610, 247
- Dong, H., Li, Z., Wang, Q. D., et al. 2016, *MNRAS*, 459, 2262
- . 2015, *MNRAS*, 451, 4126
- . 2014, *ApJ*, 785, 136
- Dopita, M. A., Jacoby, G. H., & Vassiliadis, E. 1992, *ApJ*, 389, 27
- Falcón-Barroso, J., Sánchez-Blázquez, P., Vazdekis, A., et al. 2011, *A&A*, 532, A95
- Fang, X., García-Benito, R., Guerrero, M. A., et al. 2015a, *ApJ*, 815, 69
- Fang, X., Guerrero, M. A., Miranda, L. F., et al. 2015b, *MNRAS*, 452, 2445
- Fang, X., Zhang, Y., García-Benito, R., Liu, X.-W., & Yuan, H.-B. 2013, *ApJ*, 774, 138
- Fang, X., García-Benito, R., Guerrero, M. A., et al. 2018, *ApJ*, 853, 50
- Ferland, G. J., Korista, K. T., Verner, D. A., et al. 1998, *PASP*, 110, 761
- Gil de Paz, A., Boissier, S., Madore, B. F., et al. 2007, *ApJS*, 173, 185
- Halliday, C., Carter, D., Bridges, T. J., et al. 2006, *MNRAS*, 369, 97
- Heisler, J., Tremaine, S., & Bahcall, J. N. 1985, *ApJ*, 298, 8
- Herrmann, K. A., & Ciardullo, R. 2009, *ApJ*, 705, 1686
- Herrmann, K. A., Ciardullo, R., Feldmeier, J. J., & Vinciguerra, M. 2008, *ApJ*, 683, 630
- Jacoby, G. H., & Ciardullo, R. 1999, *ApJ*, 515, 169
- Jacoby, G. H., Ciardullo, R., Booth, J., & Ford, H. C. 1989, *ApJ*, 344, 704
- Jacoby, G. H., Ford, H., & Ciardullo, R. 1985, *ApJ*, 290, 136

- Kauffmann, G., Heckman, T. M., White, S. D. M., et al. 2003, MNRAS, 341, 33
- Kent, S. M. 1989, AJ, 97, 1614
- Kong, A. K. H., Sjouwerman, L. O., Williams, B. F., Garcia, M. R., & Dickel, J. R. 2003, ApJ, 590, L21
- Kwitter, K. B., Lehman, E. M. M., Balick, B., & Henry, R. B. C. 2012, ApJ, 753, 12
- Kwok, S. 2000, The Origin and Evolution of Planetary Nebulae
- Li, Z., & Wang, Q. D. 2007, ApJ, 668, L39
- Li, Z., Wang, Q. D., & Wakker, B. P. 2009, MNRAS, 397, 148
- Longobardi, A., Arnaboldi, M., Gerhard, O., & Hanuschik, R. 2015a, A&A, 579, A135
- Longobardi, A., Arnaboldi, M., Gerhard, O., & Mihos, J. C. 2015b, A&A, 579, L3
- Mathews, W. G. 1990, ApJ, 354, 468
- McConnachie, A. W., Irwin, M. J., Ferguson, A. M. N., et al. 2005, MNRAS, 356, 979
- McMillan, R., Ciardullo, R., & Jacoby, G. H. 1994, AJ, 108, 1610
- Merrett, H. R., Merrifield, M. R., Douglas, N. G., et al. 2006, MNRAS, 369, 120
- Miszalski, B., Mikołajewska, J., & Udalski, A. 2013, MNRAS, 432, 3186
- Morisset, C., Delgado-Inglada, G., & Flores-Fajardo, N. 2015, Rev. Mexicana Astron. Astrofis., 51, 103
- Nagao, T., Maiolino, R., & Marconi, A. 2006, A&A, 459, 85
- Osterbrock, D. E., & Ferland, G. J. 2006
- Parker, Q. A., Bojicic, I., & Frew, D. J. 2016, ArXiv e-prints, arXiv:1612.00167
- Pastorello, N., Sarzi, M., Cappellari, M., et al. 2013, MNRAS, 430, 1219
- Peng, E. W., Ford, H. C., & Freeman, K. C. 2004, ApJ, 602, 685
- Richer, M. G., Stasińska, G., & McCall, M. L. 1999, A&AS, 135, 203
- Rosenfield, P., Johnson, L. C., Girardi, L., et al. 2012, ApJ, 755, 131
- Saglia, R. P., Fabricius, M., Bender, R., et al. 2010, A&A, 509, A61
- Sanders, N. E., Caldwell, N., McDowell, J., & Harding, P. 2012, ApJ, 758, 133

- Sarzi, M., Mamon, G. A., Cappellari, M., et al. 2011, MNRAS, 415, 2832
- Schlafly, E. F., & Finkbeiner, D. P. 2011, ApJ, 737, 103
- Schönberner, D., Jacob, R., Sandin, C., & Steffen, M. 2010, A&A, 523, A86
- Storey, P. J., & Hummer, D. G. 1995, MNRAS, 272, 41
- Tamm, A., Tempel, E., Tenjes, P., Tihhonova, O., & Tuvikene, T. 2012, A&A, 546, A4
- Walsh, J. R., Rejkuba, M., & Walton, N. A. 2015, A&A, 574, A109
- Walsh, J. R., Walton, N. A., Jacoby, G. H., & Peletier, R. F. 1999, A&A, 346, 753
- Wilson, O., & Woolley, R. 1970, MNRAS, 148, 463
- Yuan, H.-B., Liu, X.-W., Huo, Z.-Y., et al. 2010, Research in Astronomy and Astrophysics, 10, 599

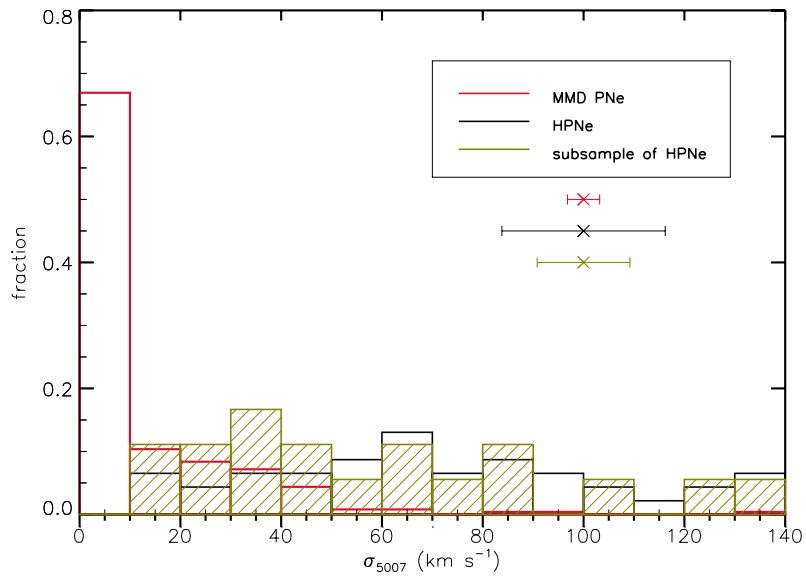


Fig. 11.— The fractional distribution of the intrinsic dispersion of the [O III] line, for the MMD PNe (red), all HPNe (black), and a subset of HPNe with S/N greater than 10 in [O III] (green).